International Journal for Housing Science and Its Applications
Publish August 10, 2025. Volume 46, Issue 4 Pages 7850-7863

https://doi.org/10.70517/ijhsa464676

CNN-enabled bird flight aerodynamic simulation and optimization model construction

Zhan Zhang[1,*]
[1] Faculty of Natural, Mathematical and Engineering Sciences, King's College London, London, WC2R 2LS, United Kingdom
Corresponding authors: (e-mail: zz2481290560@163.com).

Abstract Aerodynamics, as an ancient discipline, has always played a significant role in fields such as aerospace, shipbuilding, and wind power generation. Rapid and accurate solutions to aerodynamic problems have long been a goal pursued by researchers. In light of this, this paper distills the form of bird wing flapping motion and the mechanisms behind high lift generation, exploring the underlying principles of how wing flapping affects aerodynamic forces. Subsequently, by integrating numerical simulation, wind tunnel testing, and flight test data, the paper establishes an empirical formula for the correlation between shock-boundary layer interaction forces/thermal loads in ground-to-air conditions, corrects the pressure-thermal flux relationship, and confirms the objective existence of low-frequency oscillations in separation bubbles under real flight conditions. Finally, the paper introduces convolutional neural networks (CNNs) to conduct experiments on wing profile aerodynamic performance prediction based on CNNs. The study shows that by reasonably arranging the network structure and optimizing hyperparameters, the convolutional neural network can achieve high accuracy in predicting the lift-to-drag ratio of airfoils. The relative error distributions of the validation set and test set are almost consistent, with approximately 90% of the samples having a relative error below 1%. Thus, the model in this paper has high accuracy and can rapidly and accurately predict the lift-to-drag ratio of unknown airfoils.

Index Terms flapping-wing flight, convolutional neural network, aerodynamics, bird flight

I. Introduction

As aviation technology continues to evolve, the primary trends in aviation development—and the goals pursued by aircraft designers—include enhancing lift, reducing drag, minimizing structural mass, improving comfort and safety, and lowering energy consumption, noise levels, and environmental impact [1]-[4]. Although aircraft designed by mimicking bird-inspired designs have far surpassed birds in terms of speed, altitude, and flight range, modern aircraft are still far from matching birds in terms of lightness, agility, efficiency, and low energy consumption [5]-[7]. Traditional aircraft configurations include fixed-wing and rotorcraft, which primarily mimic and enhance the macro-aerodynamic or morphological characteristics of flying organisms, utilizing rigid structures for load-bearing [8], [9]. This traditional aircraft design theory, based on a macro-aerodynamic perspective, has pushed performance improvements such as lift enhancement, drag reduction, noise reduction, and weight reduction to near their limits [10], [11]. This has led to a technical bottleneck in achieving breakthrough improvements in the overall performance of aircraft using current relatively mature aerodynamic and structural design methods [12]. Especially when the Reynolds number drops below 105, unmanned aerial vehicles face numerous issues such as reduced aerodynamic efficiency due to decreased propeller efficiency and wing lift-to-drag ratio, flight control difficulties due to reduced aerodynamic efficiency of control surfaces, and poor wind stability due to low inertia [13]-[16]. However, birds possess highly efficient adaptive endurance capabilities, and their aerodynamic drag reduction, lift enhancement, and noise reduction mechanisms hold significant implications for aircraft aerodynamic design [17], [18]. Additionally, biomimetic variable-geometry design and wing shape changes inspired by birds' ability to alter flight posture and fold their wings during landing hold significant implications for future aircraft variants and efficient folding mechanisms [19]-[21]. Therefore, to address aerodynamic and control challenges faced by artificial aircraft at low Reynolds numbers, biomimetic flight technology inspired by birds has developed rapidly over the past two decades.

During gliding flight, birds' wings generate significant lift. Inspired by this phenomenon, numerous scholars have studied aerodynamics under different aircraft wing configurations, making important contributions to improving aircraft performance. Wang, F., et al. introduced the biomimetic principles of flapping-wing aircraft and used Xflow software to simulate the aerodynamic forces generated by the flapping motion of the aircraft, confirming the effectiveness of the bird-inspired flapping-wing and flapping-tail design through motion tests [22]. Changchuan, X. I. E., and others employed simple numerical calculation methods to investigate the aerodynamic characteristics of

bird flight. The leading-edge vortices generated by their wings are a key manifestation of lift and thrust in bird-inspired flapping-wing aircraft, and also serve as the background basis for high-efficiency wing configurations, kinematic designs, and deformation methods [23]. Colognesi, V., et al. combined a biomechanical model based on bird anatomy with an aerodynamic model to construct a multi-physics computational framework, providing aerodynamic references for flapping-wing aircraft through lift line methods and control volume analysis [24]. Liu, T et al. proposed the development of a simulation model based on bird flight for the design optimization of flapping-wing drones and micro-air vehicles. By analyzing data on bird body structure, wing shape, motion characteristics, and aerodynamics, they provided effective insights for design [25]. Xie, H et al. designed an efficient and universal numerical aerodynamic model applicable to general three-dimensional geometric shapes in potential flow. Combined with a general rigid body simulator, it enables natural and real-time aircraft motion simulation, providing important assistance for the design of flyable gliders [26]. Ruiz, C., et al. analyzed and modeled the unsteady aerodynamic characteristics generated by flapping-wing aircraft during the flapping process using three-dimensional computational fluid dynamics. By inputting observed aerodynamic load data into a finite memory Volterra model, they accurately predicted the force and torque characteristics generated by flapping [27]. Roccia, B. A. proposed a joint simulation strategy based on a numerical simulation framework, applying structural and aerodynamic models to simulate flying insects and small birds, providing references for wing deformation patterns in micro-air vehicles [28]. Soni, A. and Tiwari, S. conducted a numerical study on the aerodynamic characteristics of non-flapping flight in birds and introduced three-dimensional computational tools to investigate the key factors affecting airflow characteristics in different wing types, providing guidance for aircraft wing design [29].

This paper first explores the principles of flapping flight, analyzes and distills the forms and mechanisms of birds, summarizes the mechanisms by which flapping flight affects aerodynamic forces, and provides an overview of aerodynamics. Subsequently, three major methods were comprehensively employed to study the fundamental flow problems of high-speed shock-boundary layer interaction, establishing empirical formulas for the correlation between shock-boundary layer interaction forces/thermal loads and ground conditions, correcting the pressure-thermal flux relationship, and for the first time confirming the objective existence of low-frequency oscillations in separation bubbles under real flight conditions. Subsequently, convolutional neural networks were introduced to conduct experiments on aerodynamic coefficient prediction and algorithm performance evaluation based on convolutional neural networks. By numerically calculating the samples to obtain aerodynamic characteristics and flow field information, a wing profile dataset was constructed. Convolutional neural networks were respectively constructed and trained for three application requirements, and the algorithm was used to optimize the hyperparameters, with accuracy analysis conducted on each network.

II. Flapping wing unsteady flow field and aerodynamic force

II. A. Basic modes of flapping flight

One of the most obvious differences between flapping-wing flight and fixed-wing flight is that during the flapping process, the flapping wing not only provides the lift necessary to maintain flight but also generates thrust. The principle by which the flapping wing profile simultaneously generates lift and thrust is illustrated in Figure 1.

When the flapping wing flies at a low constant speed V horizontally, although the angle of attack of the wing profile is 0°, the downward flapping motion of the wing generates a vertical upward velocity V_{flap} relative to the wing. The magnitude of the resultant velocity of the flapping wing relative to the stationary airflow becomes:

$$V = \sqrt{V_{\infty}^2 + V_{flap}^2} \tag{1}$$

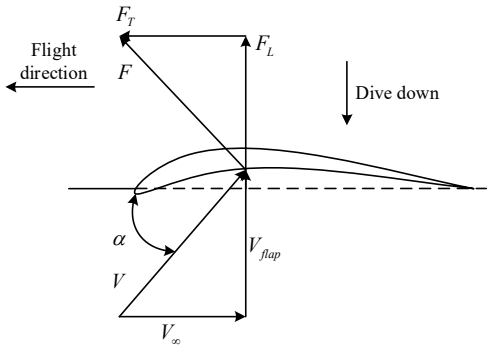

Figure 1: Aerodynamic schematic diagram of the flapping wing type

The direction of the resultant velocity is deflected upward by an angle α relative to V_∞. According to lift theory, the direction of the total aerodynamic force F on the flapping wing is perpendicular to the direction of the resultant velocity V. This load F can be decomposed into lift F_L in the vertical direction and thrust F_T in the horizontal direction.

The aerodynamic principles of fixed-wing airfoils are shown in Figure 2. When a fixed-wing aircraft flies at an angle of attack α and velocity V_∞, the airflow over the wing surface produces a downward wash effect due to the tail vortex, imparting a downward wash velocity w to the incoming flow, thereby causing the originally horizontal airflow to tilt downward. Similar to flapping wing flight, the magnitude of the resultant velocity of the airfoil relative to the stationary airflow is:

$$V = \sqrt{V_\infty^2 + w^2} \tag{2}$$

However, unlike flapping flight, this downwash effect reduces the original angle of attack, resulting in an effective angle of attack of:

$$\alpha_e = \alpha - \varepsilon \tag{3}$$

According to Joukowski's lift theory, the lift acting on the wing surface is always perpendicular to the direction of the resultant velocity V. At this point, the component of the resultant aerodynamic force in the vertical direction is the lift, and the component in the horizontal direction is the induced drag. The induced drag at this point can be regarded as the opposite direction of the thrust.

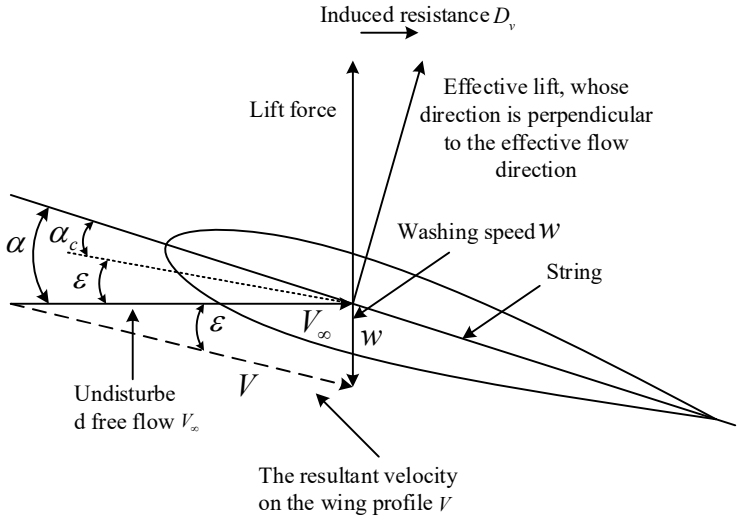

Figure 2: Aerodynamic schematic diagram of the fixed wing type

II. B.High lift mechanism of flapping flight

II. B. 1) Flapping motion of birds

Observations and analyses of flapping flight in larger birds reveal that, although flapping postures vary among species, flapping flight during level flight can generally be divided into two phases: the downward stroke and the upward stroke. A typical flapping cycle can be broken down as follows: the downward stroke is the primary phase of flapping, lasting the longest. During this phase, the primary feathers close and extend, increasing the wingspan and thereby increasing the frontal area, effectively enhancing lift. The upward phase is a passive return phase aimed at quickly restoring the wing to its highest point to initiate the next cycle, with a short duration. During this phase, the primary feathers spread apart to create gaps, allowing air to pass through rapidly and thereby reducing air resistance.

II. B. 2) The Mechanism of Lift Generation in Birds

The primary forces acting on birds during flight are lift and gravity, thrust and drag, with drag comprising pressure drag, viscous drag, and induced drag. The vertical and horizontal forces generated by the wings remain in equilibrium during steady flight or hovering [30]. The primary forces birds must overcome during flight are their own weight and drag, with weight typically exceeding drag. Consequently, the lift generated by the wings often exceeds

the drag encountered during flight. The lift-to-drag ratio is the ratio of lift to drag, and it increases with wing span. Although flapping flight consists of upward and downward wing movements, the underlying mechanics of how lift is generated through these movements are far more complex. At every moment, the shape of the wing and the aerodynamic forces generated on its surface are constantly changing. The decomposition of bird flapping movements into a two-dimensional model is shown in Figure 3, illustrating the changes in flapping angle and pitch position within a single flapping cycle.

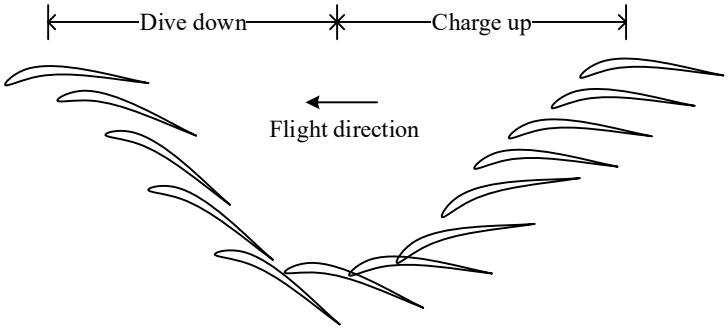

Figure 3: Changes of airfoil within one cycle

(1) Downstroke Process

This stage represents the flapping process of the wing profile from its highest point to its lowest point. It is the longest phase in the entire flapping cycle and the primary stage for generating lift and thrust. At the beginning of the downward flapping process, the bird fully extends the wing surface, maximizing the outward extension of the outer wing and slightly extending it in the forward flight direction. This creates a forward-inclined straight line at the leading edge of the wing and fully spreads the flight feathers at the trailing edge, maximizing the frontal area exposed to the wind. The inner wing surface has only a small flapping amplitude during the downward flapping process, maintaining basic up-and-down movement with a relatively slow relative airflow velocity. However, the outer wing surface extends forward and downward, with a large flapping amplitude and a relatively high relative airflow velocity. Additionally, to ensure appropriate angles of attack across different sections of the wing surface, the wing tips are tilted forward and downward at a certain angle, with the leading edge lowered and the trailing edge raised. This creates a uniformly transitioning negative twist aerodynamic surface from the wing root to the wing tip, effectively enhancing lift and preventing wing tip stall. This configuration also effectively regulates the lateral flow of air. For the outer wing surface, due to its faster flapping speed, the negative angle of attack of the wing profile increases, resulting in a larger horizontal component of aerodynamic force, with most of the horizontal thrust generated from this. During the downward flapping phase, the total vertical lift and horizontal thrust of the wing can be expressed as:

$$\begin{cases} F_L = L\cos\theta + D\sin\theta \\ F_T = L\sin\theta - D\cos\theta \end{cases} \tag{4}$$

(2) Upstroke process

This stage is a passive recovery process, the purpose of which is to quickly return the wings to their highest point and prepare for the next cycle of flapping. At the beginning of the upstroke process, birds first contract the muscles on the inner side of their wings, causing the inner wing surface to rotate upward along the wing root axis. Then, the inner wing drives the outer wing surface to also begin moving upward, folding the wings through the phase difference between the outer and inner wings during the upstroke process [31]. The movement of the outer wing surface is far more complex than the upward rotation of the inner wing surface around the wing root axis. While moving upward as a whole, the outer wing also undergoes a backward twist, lifting the leading edge, depressing the trailing edge, and bringing the wing surface together toward the rear, thereby overlapping the flight feathers. These combined movements of twisting, contracting, and overlapping help reduce the frontal area during the upward flap, thereby decreasing air resistance and negative lift, ensuring that both vertical lift and horizontal thrust remain positive throughout the entire flap cycle.

The aerodynamic forces acting on the wing surface during the upward flap are far more complex than during the downward flap. Aerodynamic characteristics not only vary along different positions along the span, but even for the same position on the wing surface, the aerodynamic forces at different moments during the upward flap are not

identical. Overall, two scenarios can be distinguished. The aerodynamic analysis of the upward swing is shown in Figure 4.

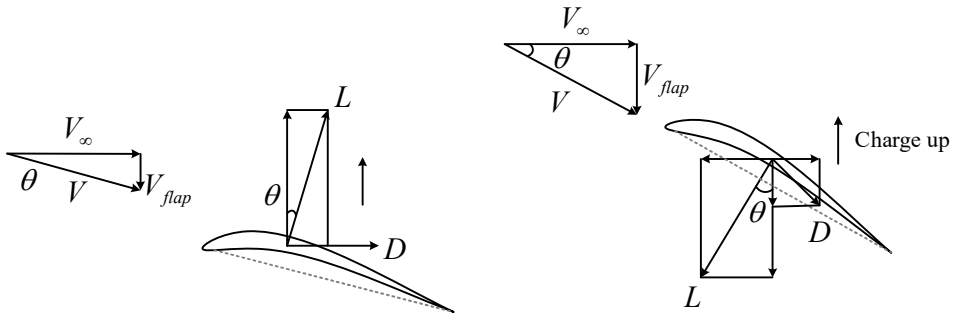

(a) Upswing situation 1 (b) Upswing situation 2

Figure 4: Aerodynamic analysis of upswing

II. C. Overview of Aerodynamics

Aerodynamics, as a branch of modern fluid mechanics, primarily studies the laws of air motion and the relative motion between air and objects. Traditional research consists of three approaches: theoretical analysis, experimental research, and numerical simulation. These three methods complement each other and collectively drive the evolution of aerodynamics.

The aerodynamic parameters used in this paper primarily include three: Mach number, angle of attack, and sideslip angle. Among these, the Mach number (Ma) is a dimensionless parameter in fluid mechanics used to represent fluid velocity. The value of the Mach number is equal to the ratio of the fluid velocity through the boundary to the local speed of sound. Its formula is:

$$Ma = \frac{u}{c} \tag{5}$$

In the equation: u is the fluid velocity through the boundary. c is the local speed of sound. This formula indicates that the Mach number can be understood as the multiple of the fluid velocity relative to the speed of sound.

The angle of attack (α), also known as the angle of attack, is the angle between the chord line of the wing section and the airflow. Within a certain acceptable range, the larger the angle of attack, the greater the lift obtained by the aircraft. However, beyond a certain range, when the angle of attack becomes too large, the aircraft will stall and lose lift.

The sideslip angle (β) is the angle between the aircraft's velocity vector and its longitudinal symmetry plane. Like the angle of attack, the sideslip angle is an important parameter for determining the aircraft's flight attitude.

III. High-speed shock wave-boundary layer interference between heaven and earth

III. A. Empirical formula for shock-boundary layer interaction force/thermal load correlation between heaven and earth

In order to realize the accurate extrapolation of SWBLI ground data to flight test of high-speed aircraft, it is necessary to analyze the space-ground difference and correlation of SWBLI. The database collects a total of 23 sets of data, including flight tests, wind tunnel tests, and numerical calculations of some typical shock boundary layer interference problems. The shape covers the zero angle of attack cone, HIFIRE-1, compression corners and column skirts, and the flight altitude covers 10 ~ 22.6 km, and the number of incoming Mach 2.9 ~ 8. In order to more accurately reveal the variation law of the mechanical-thermal load caused by SWBLI, we also obtained the force and heat distribution of the two-dimensional 34° compression corner under 24 working conditions with different Reynolds numbers, total temperature and wall temperature ratio through direct numerical simulation. By comparing and analyzing the data of nearly 50 working conditions, we get the main rules of the change of thermal load of compressive angular force: 1) When the total temperature and wall temperature ratio are fixed, the larger the Reynolds number, the smaller the size of the separation bubble, the dimensionless peak pressure and heat flux of the reattachment point, and the linear relationship between the dimensionless peak pressure and heat flux of the reattachment point and the 0.2 power of the Reynolds number. 2) When the Reynolds number and the wall temperature ratio are fixed, it can be approximated that the dimensionless pressure and heat flux are independent of the total temperature. 3) When the Reynolds number and total temperature are fixed, the larger the wall-temperature ratio, the larger the separating

bubble, but the wall-temperature ratio has little effect on the dimensionless peak pressure of the attached point. In addition, the larger the wall-to-temperature ratio, the smaller the dimensionless heat flux at the re-attachment point, and the linear relationship between the dimensionless heat flux and the wall-to-temperature ratio is approximately linear. Based on the above research, we obtained the empirical formula of SWBLI force/heat load space-ground correlation, and we verified the applicability of the above-mentioned space-ground correlation empirical relationship under different wall temperature ratios, total temperatures, Reynolds numbers and incoming Mach numbers through eight additional working conditions, and the length error of the separation zone was less than 8%, and the peak heat flow error was less than 10%. Finally, based on the wind tunnel test and the typical flight state parameters, we verified the correlation between the aerodynamic hot sky and the earth through numerical simulation, and the wind tunnel test adopted a 1:2 scale model.

Prior to this, the accuracy of the numerical simulation needed to be verified. Therefore, based on the ballistic data of the flight test model, the aerothermal environment at two measurement points upstream and inside the compression corner was calculated and compared with the flight test measurement results. The comparison between the calculated and measured temperatures at the measurement points near the compression corner is shown in Figure 5 (Figure a shows the upstream measurement point of the compression corner, and Figure b shows the internal measurement point of the compression corner). The calculated values agree well with the measured values, demonstrating the reliability of the numerical simulation. Based on the provided test conditions and flight condition parameters, numerical simulation calculations were conducted. The shock-boundary layer interaction ground-air correlation equations are shown in Figure 6 (Figures a–c represent flight test results, ground wind tunnel results, and ground-air data correlation, respectively). The figure shows the heat flux values on the symmetric surface of the compression corner region for the flight test configuration. The cold wall heat flux in the flight state (Figure a) is significantly higher than the ground test values (Figure b). Note that the ground test used a 1:2 scaled model, so the horizontal coordinate range in Figure b is half that of Figure a. However, after introducing the local Reynolds number, compressibility correction, and wall temperature correction heat flux values into the established aerodynamic-thermal ground-space correlation equation, and using the separation zone length as the reference length, Figure (c) shows that the dimensionless heat flux in the separation zone and the dimensionless heat flux at the reattachment point are essentially consistent under different conditions, with the separation onset location and separation zone size also being consistent (in Figure (c), $x^* = -1$ marks the separation onset point, and $x^* = 0$ is the corner). The above results indicate that the shock-boundary layer interaction correlation equation we established is accurate.

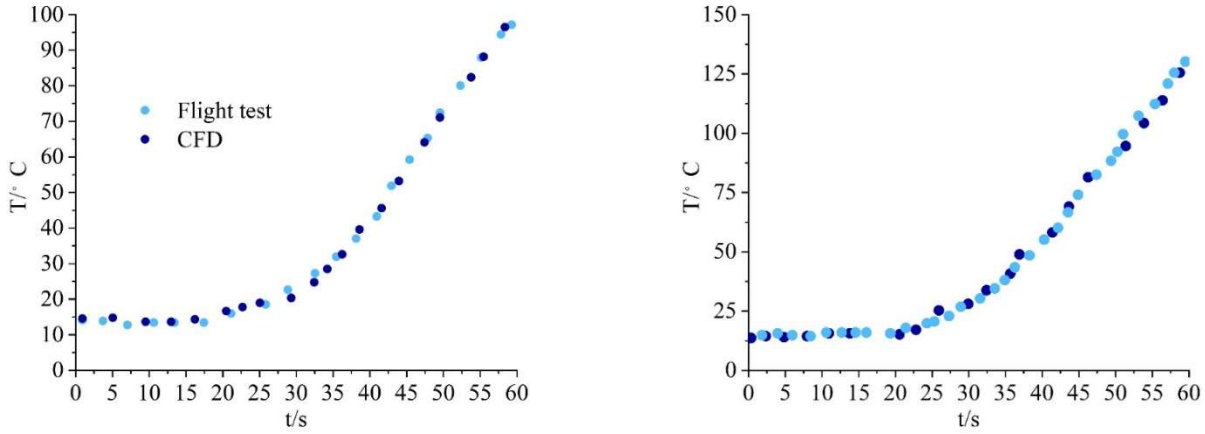

(a) Compress the measurement points upstream of the corner

(b) Compress the inner measurement points at the corners

Figure 5: Compare the calculated and measured values of the temperature

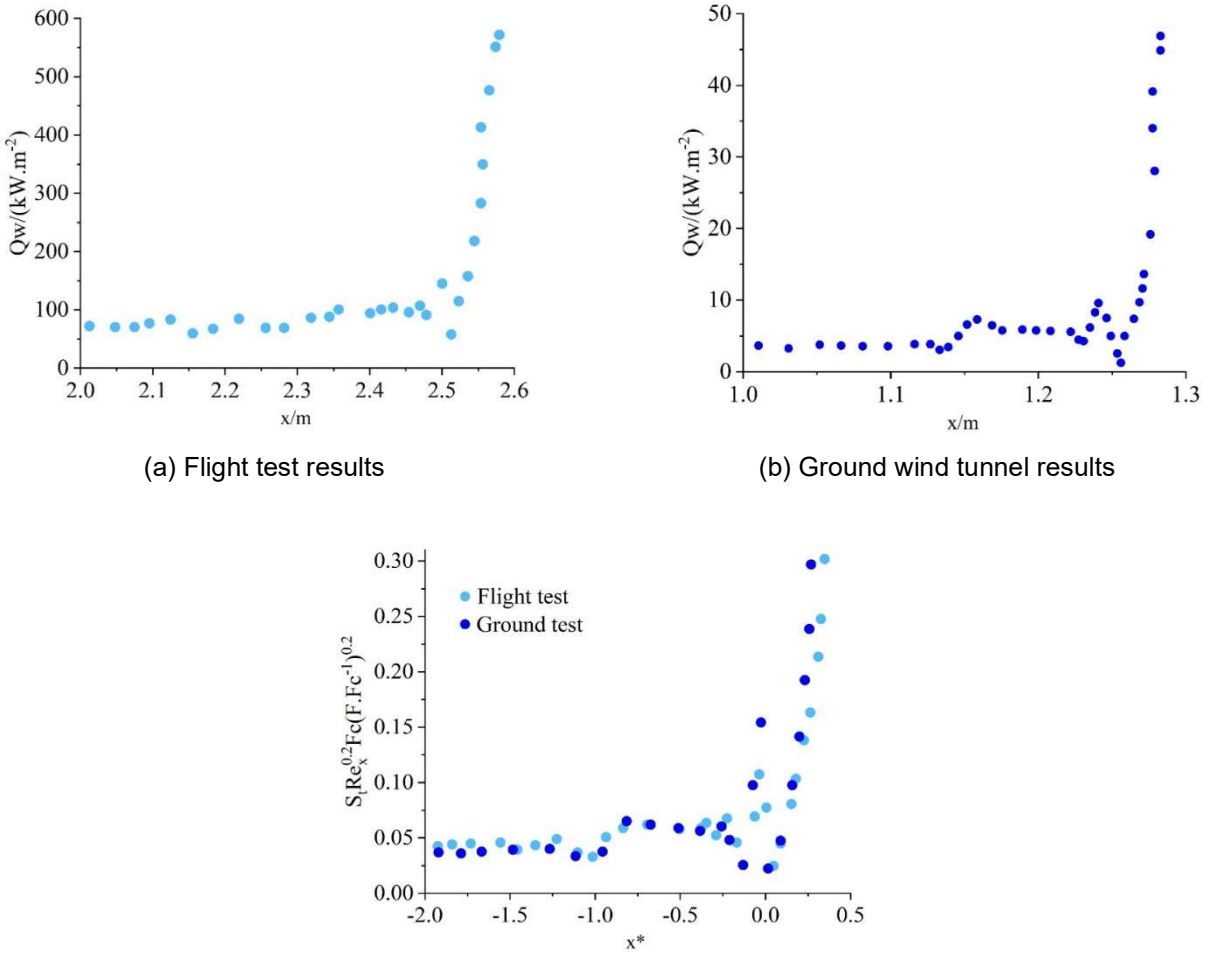

(a) Flight test results

(b) Ground wind tunnel results

(c) Data association between heaven and Earth

Figure 6: Ground and flight correlation of the wall heat flux in the SWBLI zone

III. B. Pressure-heat flow correlation

Due to the complex mechanisms underlying the unsteady effects caused by shock-turbulent boundary layer interaction and the inherent complexity of turbulence-induced heating, there is currently no reliable method for directly predicting the sharp increase in wall heat flux following shock-turbulent boundary layer interaction. However, in experiments, wall pressure is generally easier to measure than wall heat flux, and there is a qualitative similarity between the time-averaged wall heat flux and pressure along the flow direction. Therefore, wall heat flux can be indirectly predicted using pressure. The above equation is supported by a large number of experimental and computational results. However, through wind tunnel experiments involving compressive corners and oblique shock waves with incoming Mach numbers Ma_∞ = 6.5 – 13 and wall temperature ratios of 0.1 – 0.4, it was found that n = 0.85 is more appropriate under turbulent conditions. Nevertheless, the above equation has yet to be validated by flight tests. The relationship between the peak pressure and peak heat flux in the interference zone obtained from flight tests is shown in Figure 7. The results show high consistency among the three experiments, all indicating that the exponent n in the equation is 0.7. This suggests that the disturbance zone may exhibit a complex state intermediate between laminar flow (n = 0.5) and turbulent flow (n = 0.8) under flight conditions. To the authors' knowledge, this is the first flight test validation of the pressure-heat flux ratio analogy theory, which has important guiding significance. However, the value of n may also be related to the position of the sensor.

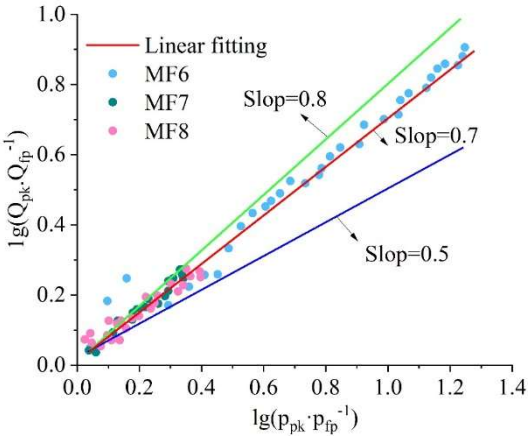

Figure 7: Relation between peak wall pressure and heat flux obtained in flight tests

III. C. Separation bubble low-frequency oscillation

Low-frequency oscillations are a typical phenomenon of SWBLI. Through multiple flight tests, we confirmed that shock-induced low-frequency oscillations also exist in the actual external flow of aircraft, with frequencies in the hundreds of hertz. The pressure pulsation PSD at the SWTBI zone wall surface at 50 s during two flight tests is shown in Figure 8. The pressure pulsation reaches a peak at a frequency of approximately 300 Hz, showing good consistency. The origin of low-frequency oscillations remains undetermined, making it a hot topic and challenge in research. However, the limited measurement capabilities of flight tests currently only allow for the determination of the spectral characteristics of low-frequency oscillations. Further research combining numerical calculations is needed to investigate the low-frequency disturbance characteristics corresponding to the conditions depicted in the figure.

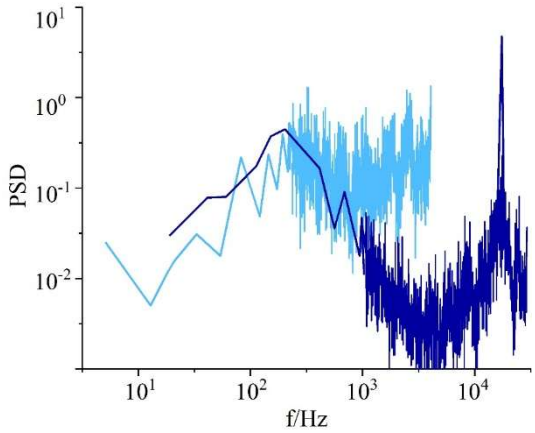

Figure 8: Pressure PSD in the SWTBI zone at 50 s for two flight tests

IV. Prediction of aerodynamic performance of airfoils based on convolutional neural networks

IV. A. Convolutional Neural Networks

IV. A. 1) Convolution Layer

(1) Convolution operation

In convolution operations, the first parameter is typically referred to as the input, and the second parameter is referred to as the convolution kernel. If a two-dimensional array I is used as the input for the convolution operation, with coordinates (m,n), the corresponding convolution kernel is denoted as K, and the feature map obtained after convolution is denoted as S, with coordinates (i,j). Then, this convolution operation can be expressed as:

$$S(i,j)=(I*K)(i,j)=\sum_{m}\sum_{n}I(m,n)K(i-m,j-n) \tag{6}$$

(2) Sparsity of Convolutional Operations

Before the advent of CNNs, all adjacent neurons in a neural network were connected, which is referred to as fully connected. The multi-layer perceptron mentioned earlier is a typical example of a fully connected neural network. Here, the output is obtained by multiplying the input by the parameters in the parameter matrix. Each parameter represents only one input-output relationship. When the number of inputs is large, the number of parameters increases accordingly. The inherent sparsity of convolution operations effectively addresses this issue [32]. In a convolutional neural network, the receptive field refers to the region of the input image that a point on the feature map can perceive. That is, the points on the feature map are calculated based on the size of the receptive field in the input image. The image on the left has a size of 1000×1000 pixels and contains 1 million neurons. If they were fully connected, meaning each neuron is connected to every pixel in the image, there would be 10^{12} connections, or 10^{12} weight parameters. However, spatial relationships in images are local, much like how humans perceive external information through the local "receptive field" of the eyes. Each neuron does not need to perceive the entire image; it only needs to perceive a local region of the image. At higher levels, by combining the perceptions of neurons that perceive different local regions, global information can be obtained. This approach reduces the number of connections, thereby reducing the number of weight parameters that need to be trained in the neural network. If the local receptive field size of the image on the right side of the figure is 10×10, then each receptive field only needs to be connected to a local image of 10×10 pixels in size. Therefore, the final 1 million neurons only have 100 million connections, i.e., 10^9 weight parameters. This reduces the number of connections by four orders of magnitude, significantly lowering the computational complexity of the neural network while improving the model's generalization ability.

(3) Parameter sharing mechanism in convolution operations

Parameter sharing refers to the use of the same parameters in multiple functions of a model. In a fully connected neural network, when calculating the results of each layer, every neuron needs to learn all the parameters, whereas in a convolutional neural network, each neuron in each layer only needs to learn the parameters on one convolution kernel. This mechanism significantly reduces the number of parameters in the neural network, further lowering the computational complexity of the neural network.

(4) Implementation of the Convolutional Layer

The convolutional layer consists of multiple feature maps, each of which is composed of multiple neurons. Each neuron is connected to a local region of the previous layer's feature map via the convolution kernel. The output of this layer is obtained by calculating the dot product between the convolution kernel weight matrix and the local region of the image. The specific calculation process is given by Equation (7):

$$y_i = \sigma(k_i * x + b_i) \quad (i = 1, 2; \cdots) \tag{7}$$

where x represents the input feature map of the convolutional layer. For a three-channel color image, its width, height, and depth are W_l, H_l, D_l, respectively. * denotes the convolution operation, k_i is the i th convolution kernel, whose width, height, and depth are F, F, D_l, b_i, respectively, denotes the corresponding bias value, σ denotes the activation function, y_i denotes the output result after the i th convolution kernel performs a convolution operation on the corresponding local image region.

At the same time, in order to better control the size of the output features, padding operations are generally performed on the input array-formatted image, typically by filling the image pixel boundaries with zeros. The primary purposes of padding are: first, to prevent certain pixels from being reused multiple times, which could weaken the information of pixels on the boundary; second, if the input feature maps have different sizes, padding can be used to ensure they are consistent in size. Finally, the width W_2 and height H_2 of the output feature image from the convolution layer are given by equation (8):

$$W_2 = \frac{W_1 - F + 2P}{S} + 1 \quad H_2 = \frac{H_1 - F + 2P}{S} + 1 \tag{8}$$

In equation (8), S is the stride length of each convolution kernel movement, typically taken as l, P is the padding dimension, typically $P = (F-1)/2$, and since multiple convolution operations can be performed simultaneously, the depth of the output feature map is determined by the number of convolution kernels.

IV. A. 2) Pooling layer

After obtaining the output feature map through the convolutional layer, a pooling layer is typically added after the convolutional layer. The primary purposes of adding a pooling layer are as follows: first, to reduce the resolution of the input feature map, decrease the number of parameters, and improve computational efficiency; second, to ensure

spatial invariance of the feature map; third, to reduce the dimensionality of the data, effectively avoiding overfitting; and fourth, to enhance the network's robustness to small deformations, distortions, and translations in the input feature map. There are two commonly used pooling methods in pooling layers: max pooling and average pooling. Max pooling, as the name suggests, selects the maximum pixel value in the downsampled image region as the pooled value for that region. Average pooling selects the average value of the pixels in the downsampled image region as the pooled value for that region.

IV. A. 3) Fully connected layer

After feature extraction through the final convolutional layer, the data is output to the first layer of the fully connected layer, where the output data is “flattened” into a one-dimensional array. Therefore, the first layer of the fully connected layer is also commonly referred to as the “Flatten” layer. In the fully connected layer, each neuron in the current layer is fully connected to all neurons in the previous layer. The output of the last layer can be passed to the output layer, and the number of specific neurons in the output layer is set according to the specific problem. To better address nonlinear problems, the number of fully connected layers is generally greater than two [33].

IV. B. Predicting experimental results

IV. B. 1) Prediction of aerodynamic coefficients of airfoils based on convolutional neural networks

Under the optimal hyperparameter combination, the model training time is approximately 15 minutes. The loss function change curves for the training set and validation set during training are shown in Figure 9. At the beginning of training, the loss is relatively high, then it decreases rapidly, and finally stabilizes gradually. When convergence is achieved, the training set loss is very small, approaching zero, while the validation set loss is slightly higher but remains below 5×10^{-5}. Based on the trend of the loss function, it can be concluded that the model has high prediction accuracy, no overfitting, and good generalization performance.

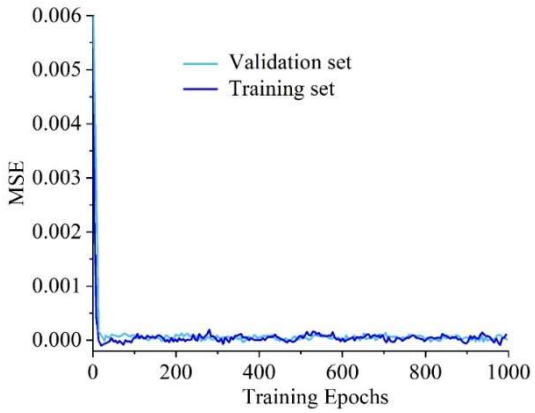

Figure 9: The variation curve of the loss function during the training process of CNN1

Under the optimal hyperparameter combination, the network model was evaluated for performance after 1000 training iterations. To more intuitively measure the model's prediction error, the relative error (RE) defined by the formula was used as a metric. The prediction time for a single sample was less than 1 second, and the lift-to-drag ratio prediction results are shown in Figure 10. where the horizontal axis represents the CFD calculation values and the vertical axis represents the CNN prediction values. The closer the scatter points are to the 45° line, the smaller the error between the prediction values and the actual values, indicating higher prediction accuracy of the model. As shown in the figure, for both the validation set and the test set, the prediction values and actual values are very close, with most points concentrated along the 45° line, and all points falling within the ±6% error margin. The relative error of lift-to-drag ratio predictions is shown in Figure 11. It can be seen that the relative error distributions for the validation set and test set are almost identical. Except for a few samples with relatively large relative errors in lift-to-drag ratio predictions, the relative errors for the remaining samples are small, with approximately 90% of samples having relative errors below 1%. In summary, the trained network model has high accuracy and can rapidly and accurately predict the lift-to-drag ratio for unknown wing profiles.

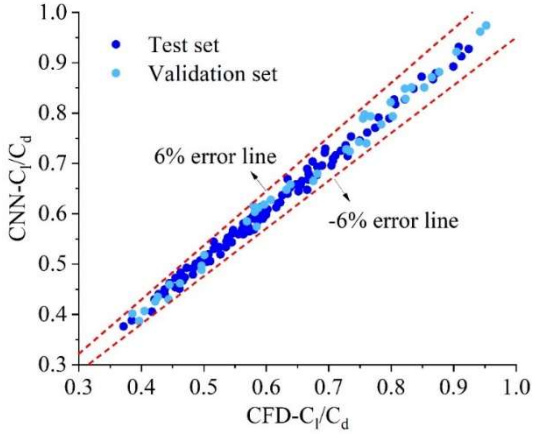

Figure 10: Prediction result of lift-to-drag ratio

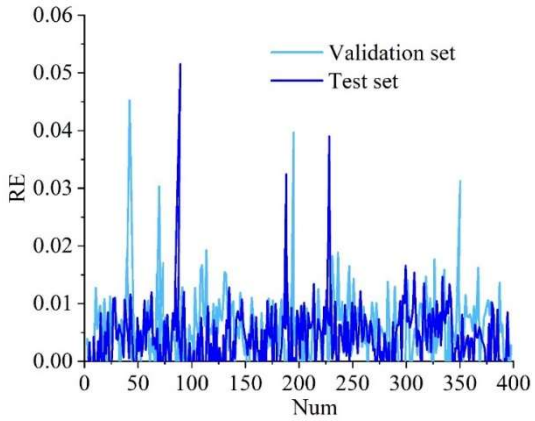

Figure 11: Relative error of lift-to-drag ratio prediction

IV. B. 2) Convolutional Neural Network Performance Evaluation

The statistical characteristics of the MAE for the validation set and test set are shown in Table 1. The mean values of the mean absolute error for the validation set and test set are 0.00211 and 0.00208, respectively. Due to the presence of some samples with relatively large prediction errors, the maximum mean absolute errors for the validation set and test set are 0.00902 and 0.01052, respectively. Therefore, the standard deviations of the mean absolute errors for the validation set and test set are relatively large, at 0.00121 and 0.00102, respectively.

Table 1: The statistical characteristics of MAE in the verification set and the test set

	Mean value	Standard deviation	Maximum value
Verification set	0.00211	0.00121	0.00902
Test set	0.00208	0.00102	0.01052

The statistical characteristics of the validation set and test set MSE are shown in Table 2. Individual sample errors are relatively large, such as the maximum mean square deviation of 1.26×10^{-3} in the validation set and 4.39×10^{-4} in the test set. The mean values of the mean square deviation of the validation set and test set are 3.51×10^{-5} and 2.62×10^{-5}, respectively.

Table 2: The statistical characteristics of MSE in the verification set and the test set

	Mean value	Standard deviation	Maximum value
Verification set	3.51×10^{-5}	8.88×10^{-5}	1.26×10^{-3}
Test set	2.62×10^{-5}	5.12×10^{-5}	4.39×10^{-4}

The mean and standard deviation distributions of the absolute errors on the upper and lower surfaces of the validation set and test set are shown in Figure 12 (Figure a shows the mean, and Figure b shows the standard deviation). It can be seen that the distribution patterns of the mean and standard deviation for the validation set and test set are generally consistent. The overall mean error on the lower surface is relatively small, fluctuating around 0.001. The mean error of the upper surface is greater than that of the lower surface, especially in the 43% to 70% chord length range. Due to the influence of shock waves, the mean error at each point significantly increases, reaching a peak at approximately 58% chord length, with a maximum value approaching 0.03. The distribution of standard deviations is similar to that of means. Positions with larger means correspond to larger standard deviations. The standard deviation of the lower surface is small, approximately 0.002, while the upper surface has larger overall values, especially in the 45% to 70% chord length range, where the standard deviation of errors at each point significantly increases, with a maximum value reaching 0.027.

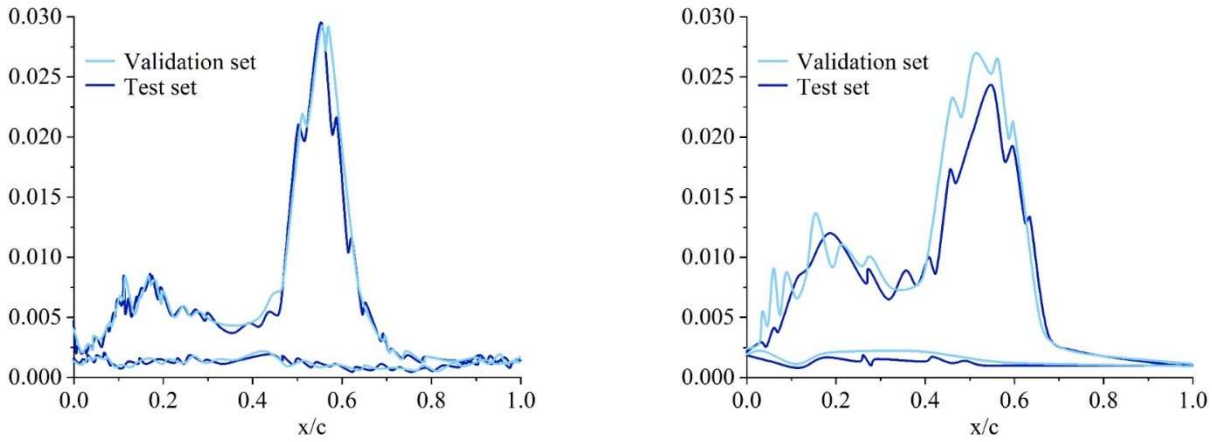

(a) Mean value (b) Standard deviation

Figure 12: The mean and standard deviation distributions of absolute error

Figure 13 shows a comparison between the CNN prediction values and CFD calculation values for the surface pressure coefficients of some samples in the test set. For different wing shapes, the convolutional neural network model trained can achieve good prediction of the surface pressure distribution, demonstrating good model generalization.

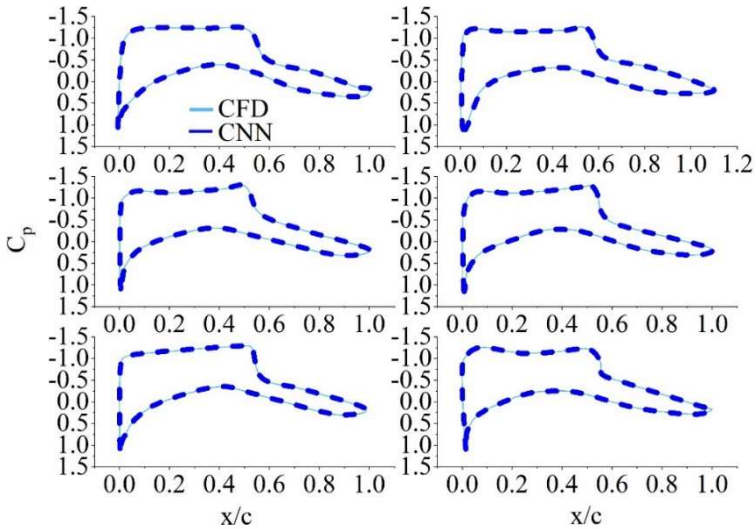

Figure 13: Comparison between the predicted values of CNN and the calculated values

V. Conclusion

This paper investigates the prediction and optimization design of aerodynamic coefficients for bird wing profiles using convolutional neural networks. The main conclusions are as follows:

In the shock-boundary layer interaction space-time correlation equation, the heat flux on the cold wall during flight is significantly higher than the ground test values. However, after introducing local Reynolds number, compressibility correction, and wall temperature correction heat flux values into the established aerodynamic-thermal space-time correlation equation, The dimensionless heat flux in the separation zone and the dimensionless heat flux at the reattachment point are essentially consistent under different conditions, indicating that the shock-boundary layer interaction ground-related correlation equation is accurate.

In experiments verifying the mean and standard deviation distributions of absolute errors on the upper and lower surfaces in the validation and test sets, it was found that the distribution patterns of the mean and standard deviation in the validation and test sets are basically consistent. The overall mean error on the lower surface is small, fluctuating around 0.001, indicating that the algorithm's performance is good.

References

[1] Zhang, T. T., Wang, Z. G., Huang, W., & Yan, L. (2018). A review of parametric approaches specific to aerodynamic design process. Acta Astronautica, 145, 319-331.

[2] Faggiano, F., Vos, R., Baan, M., & Van Dijk, R. (2017). Aerodynamic design of a flying V aircraft. In 17th AIAA Aviation Technology, Integration, and Operations Conference (p. 3589).

[3] Liem, R. P., Martins, J. R., & Kenway, G. K. (2017). Expected drag minimization for aerodynamic design optimization based on aircraft operational data. Aerospace Science and Technology, 63, 344-362.

[4] Liou, M. F., Kim, H., Lee, B., & Liou, M. S. (2019). Aerodynamic design of integrated propulsion–airframe configuration of a hybrid wing body aircraft. Shock Waves, 29(8), 1043-1064.

[5] Wang, M., & Liu, X. (2019). Numerical investigation of aerodynamic and acoustic characteristics of bionic airfoils inspired by bird wing. Proceedings of the Institution of Mechanical Engineers, Part G: Journal of Aerospace Engineering, 233(11), 4004-4016.

[6] Ma, D., Song, B., Gao, S., Xue, D., & Xuan, J. (2024). Designing efficient bird-like flapping-wing aerial vehicles: Insights from aviation perspective. Bioinspiration & Biomimetics, 19(6), 061001.

[7] Zhang, X., Cheng, G., & Chen, G. (2023). A New Type Bionic Foldable Wing Design for High Maneuverable Unmanned Aerial Vehicle. Applied Sciences, 13(14), 8345.

[8] Xue, D., Song, B., Song, W., Yang, W., Xu, W., & Wu, T. (2019). Computational simulation and free flight validation of body vibration of flapping-wing MAV in forward flight. Aerospace Science and Technology, 95, 105491.

[9] Shen, Y., Xu, Y., Huang, W., Shang, C., & Shi, Q. (2025). Effect of coupled wing motion on the aerodynamic performance during different flight stages of pigeon. Cyborg and Bionic Systems, 6, 0200.

[10] Mills, R., Hildenbrandt, H., Taylor, G. K., & Hemelrijk, C. K. (2018). Physics-based simulations of aerial attacks by peregrine falcons reveal that stooping at high speed maximizes catch success against agile prey. PLoS Computational Biology, 14(4), e1006044.

[11] Wüest, V., Jeger, S., Feroskhan, M., Ajanic, E., Bergonti, F., & Floreano, D. (2024). Agile perching maneuvers in birds and morphing-wing drones. Nature Communications, 15(1), 8330.

[12] Bao, H., Yang, W., Ma, D., Song, W., & Song, B. (2020). Numerical simulation of flapping airfoil with alula. International Journal of Micro Air Vehicles, 12, 1756829320977989.

[13] Omar, A., Rahuma, R., & Emhemmed, A. (2020). Numerical Investigation on Aerodynamic Performance of Bird's Airfoils. Journal of Aerospace Technology and Management, 12, e4620.

[14] Shams Taleghani, A., & Torabi, F. (2025). Recent developments in aerodynamics. Frontiers in Mechanical Engineering, 10, 1537383.

[15] Liu, D., Song, B., Yang, W., Yang, X., Xue, D., & Lang, X. (2021). A brief review on aerodynamic performance of wingtip slots and research prospect. Journal of Bionic Engineering, 18, 1255-1279.

[16] Qiuhong, L., Jiandong, H., Chong, W., Yuan, C., & Bokai, Z. (2025). Study on the Aerodynamic Characteristics of Bird-like Flapping Wings Under Multi-degree-of-Freedom Conditions. International Journal of Aeronautical and Space Sciences, 1-9.

[17] Yuan, L., & Yubo, Z. (2024, June). Overview of research status and key technologies of bionic flapping wing aircraft. In Journal of Physics: Conference Series (Vol. 2784, No. 1, p. 012002). IOP Publishing.

[18] Nawi, M. R. M., & Azhar, M. S. A. (2018). Aerodynamics Performance of Barn Swallow Bird at Top Speed: A Simulation Study. Journal of Mechanical Engineering (JMechE), (5), 1-15.

[19] Beaumont, F., Murer, S., Bogard, F., & Polidori, G. (2025). Aerodynamics of Flight Formations in Birds: A Quest for Energy Efficiency. Birds, 6(2), 15.

[20] Zhao, M., Zou, Y., Fu, Q., & He, W. (2021). Effects of airfoil on aerodynamic performance of flapping wing. Biomimetic Intelligence and Robotics, 1, 100004.

[21] Yang, Y., & Su, H. (2018). Aerodynamic simulation of multi-DOF flapping-wing air vehicle of bird-like based on XFlow software. Journal of System Simulation, 30(6), 2162-2167.

[22] Wang, F., Gong, J., Guo, S., Ban, C., Wei, W., & Long, Y. (2025). Design and aerodynamic performance simulation of bird like flapping-wing aircraft based on spatial bias mechanism. International Journal of Intelligent Robotics and Applications, 1-17.

[23] Changchuan, X. I. E., Nongyue, G. A. O., Yang, M. E. N. G., Yue, W. U., & Chao, Y. A. N. G. (2023). A review of bird-like flapping wing with high aspect ratio. Chinese Journal of Aeronautics, 36(1), 22-44.

[24] Colognesi, V., Ronsse, R., & Chatelain, P. (2021). Model coupling biomechanics and fluid dynamics for the simulation of controlled flapping flight. Bioinspiration & Biomimetics, 16(2), 026023.

[25] Liu, T., Wang, S., Liu, H., & He, G. (2023). Engineering perspective on bird flight: Scaling, geometry, kinematics and aerodynamics. Progress in Aerospace Sciences, 142, 100933.

[26] Xie, H., Igarashi, T., & Miyata, K. (2018). Precomputed panel solver for aerodynamics simulation. ACM Transactions on Graphics (TOG), 37(2), 1-12.
[27] Ruiz, C., Acosta, J. Á., & Ollero, A. (2022). Aerodynamic reduced-order Volterra model of an ornithopter under high-amplitude flapping. Aerospace Science and Technology, 121, 107331.
[28] Roccia, B. A., Preidikman, S., & Balachandran, B. (2017). Computational dynamics of flapping wings in hover flight: a co-simulation strategy. AIAA Journal, 55(6), 1806-1822.
[29] Soni, A., & Tiwari, S. (2019). Three-dimensional numerical study on aerodynamics of non-flapping bird flight. Sādhanā, 44, 1-15.
[30] Jinze Liang,Mengzong Zheng,Tianyu Pan,Guanting Su,Yuanjun Deng,Mengda Cao & Qiushi Li. (2025). Development of a Dragonfly-Inspired High Aerodynamic Force Flapping-Wing Mechanism Using Asymmetric Wing Flapping Motion. Biomimetics,10(5),309-309.
[31] Peiqi Li,Zhiwei Ai & Mufan Zhang. (2025). Optimized actuator design for flapping-wing robots: A multi-objective approach to mimic natural flapping dynamics. Advances in Mechanical Engineering,17(4).
[32] Mikhail PETROV & Sofia ZIMINA. (2024). An application of space-filling curves to improve results of turbulent aerodynamics modeling with convolutional neural networks. Chinese Journal of Aeronautics,37(2),81-92.
[33] Yu Xinyang & Wu Teng. (2023). Simulation of unsteady flow around bluff bodies using knowledge-enhanced convolutional neural network. Journal of Wind Engineering & Industrial Aerodynamics,236.